Research Square

Preprints are preliminary reports that have not undergone peer review.
They should not be considered conclusive, used to inform clinical practice,
or referenced by the media as validated information.

Thermal Response and Aging Behavior of Lithium-ion Batteries for New-energy Locomotives under Complex Operating Conditions

Kui Chen

kchen@swjtu.edu.cn

Southwest Jiaotong University

Xiaoying Zheng

Southwest Jiaotong University

Huai Gao

Southwest Jiaotong University

Mingchuan Tang

Southwest Jiaotong University

Hongjie Wang

Southwest Jiaotong University

Zhou Long

Southwest Jiaotong University

Fan Wu

Southwest Jiaotong University

Guoqiang Gao

Southwest Jiaotong University

Guangning Wu

Southwest Jiaotong University

Research Article

Keywords: lithium-ion battery, multi-physics coupling, thermal behavior, aging behavior, SEI film growth model

Posted Date: June 4th, 2026

DOI: https://doi.org/10.21203/rs.3.rs-9790028/v1

License: This work is licensed under a Creative Commons Attribution 4.0 International License.
Read Full License

Additional Declarations: No competing interests reported.

Thermal Response and Aging Behavior of Lithium-ion Batteries for New-energy Locomotives under Complex Operating Conditions

Kui Chen [1,2], Xiaoying Zheng [1], Huai Gao [1], Mingchuan Tang [2], Hongjie Wang [2], Zhou Long [1], Fan Wu [1], Guoqiang Gao [1], Guangning Wu [1]

(1. College of Electrical Engineering, Southwest Jiaotong University, Chengdu 611756, Sichuan Province, China;
2. Yibin Research Institute, Southwest Jiaotong University, Yibin 644000, Sichuan Province, China.)

Corresponding author: Kui Chen; Email Address: kchen@swjtu.edu.cn

Abstract: Lithium-ion batteries have become a mainstream energy storage technology owing to their high energy density and long cycle life. however, their thermal safety and aging issues remain critical challenges to reliable operation. In this study, an electrochemical-thermal-SEI film growth multi-physics coupled model is developed to simulate and analyze the thermal and aging behaviors of a single lithium-ion cell under different charge/discharge C-rates and ambient temperature conditions. The spatial nonuniformity of the coupled thermal-aging response within the cell is further analyzed. The results show that, as the discharge rate increases, the terminal voltage decreases more rapidly, the discharge duration is shortened, the discharge curves after cycling shift leftward, and the available capacity declines. Under the high-rate 4C condition, the temperature rise rate is 2.26 times that under the low-rate condition, and the increase in SEI film thickness is 2.23 times that under the low-rate condition, indicating that high-rate operation substantially intensifies electrochemical polarization, internal heat generation, and SEI-related side reactions. Ambient temperature also has a pronounced influence on battery aging: high-temperature operation leads to severe SOH degradation and a marked increase in the temperature nonuniformity coefficient. These findings reveal the coupled effects of rate, temperature, and spatial distribution on battery aging, providing a theoretical basis for thermal management optimization and lifetime prediction of traction batteries in new-energy locomotives.

Keywords: lithium-ion battery; multi-physics coupling; thermal behavior; aging behavior; SEI film growth model

1 Introduction

Among various energy storage technologies, including pumped hydro storage, compressed-air energy storage, and flywheel energy storage, electrochemical energy storage is regarded as one of the most promising routes because of its fast response, high efficiency, flexible deployment, and broad applicability [1]. Lithium-ion batteries, in particular, have been widely used in consumer electronics,

new-energy vehicles, and grid peak regulation due to their high energy density, high power density, long cycle life, and low self-discharge rate [2][3][4]. They have become an essential foundation for energy transition and transport electrification, and their reliability and safety have therefore attracted increasing attention. In the rail transit sector, the growing demand for green, low-carbon, and intelligent railway transportation has accelerated the development of new-energy locomotives as an important alternative to conventional diesel locomotives and as an upgrade solution for traction equipment on non-electrified lines. In recent years, accidents caused by thermal runaway of lithium-ion batteries have occurred frequently, especially in energy storage stations and new-energy vehicles [5],[6]. Under high-rate charge-discharge, elevated temperature, overcharge or overdischarge, poor heat dissipation, or long-term aging, internal side reactions and heat generation are significantly intensified. If the generated heat cannot be dissipated in time, interfacial instability, lithium plating, separator shrinkage, and even thermal runaway may occur [7],[8]. Aged batteries, characterized by higher internal resistance, more pronounced polarization, and more intricate temperature distributions, exhibit greater unpredictability in their lifespan prediction [9],[10]. These issues are particularly important for traction batteries in new-energy locomotives. On the one hand, locomotive operation involves typical high-power scenarios such as starting acceleration, uphill traction, heavy-load operation, frequent start-stop cycles, and regenerative braking, requiring the battery to withstand large power fluctuations and high instantaneous rates. On the other hand, locomotives may operate across a wide range of environments, including high and low temperatures, long-duration continuous service, and constrained heat-dissipation conditions. Compared with ordinary vehicle batteries, traction batteries for new-energy locomotives differ markedly in power demand, service duration, load fluctuation, and safety redundancy; therefore, conclusions developed for general automotive batteries cannot be directly applied to their thermal management and lifetime assessment.

Thermal behavior and aging behavior are not independent but are strongly coupled [11]. Temperature directly regulates the rates of electrochemical reactions and side reactions by affecting key parameters such as reaction rate constants, diffusion coefficients, and ionic/electronic conductivity. Conversely, aging modifies impedance characteristics, the inventory of active lithium, and heat-generation distribution [12],[13], thereby feeding back into the thermal response of the battery. This coupled thermal-aging relationship governs not only the lifetime evolution of a single cell but also the

development of inconsistency within battery packs and the safety behavior of the overall system.

Considerable progress has been made in the study of electrochemical, thermal, and aging behavior of lithium-ion batteries. Zeyang Geng et al. [14] introduced a novel implementation of a widely used pseudo-two-dimensional (P2D) lithium-ion battery model based on a transmission-line circuit structure. They simulated the discharge process of NMC/graphite lithium-ion batteries under different currents and showed that the circuit-model results, including terminal voltage and concentration distribution, agreed closely with those obtained from COMSOL Multiphysics simulations, demonstrating the interaction between physics-based and equivalent circuit models. Y. Li et al. [15] developed an electrochemical-thermal-aging coupled model incorporating lithium plating and solid electrolyte interphase (SEI) growth, investigated the coupled effects of state of health (SOH), charging C-rate, and ambient temperature on the lithium-plating boundary, and further constructed three-dimensional safety boundaries for lithium plating under different operating conditions. Luo et al. [16] proposed a physics-based electrochemical-thermal-mechanical-side reaction (ETMS) coupled aging model to describe multi-physics coupling during battery cycling. Their ETMS model demonstrated that high-current charging accelerates nonuniform side reactions, improves the understanding of battery aging behavior, enhances model applicability under dynamic conditions, and provides abundant physical information for battery health evaluation and remaining useful life prediction.

Under complex operating conditions, high-rate discharge intensifies polarization and heat generation, elevated ambient temperature accelerates SEI film growth and active lithium loss, and long-term cycling further increases internal resistance and aggravates heat accumulation. These processes form a mutually reinforcing coupled degradation pathway among rate, temperature, and aging. Therefore, for new-energy locomotive applications, a systematic investigation of the thermal response and aging behavior of lithium-ion batteries under complex operating conditions is essential not only for revealing the performance degradation mechanisms of traction batteries, but also for providing a theoretical basis for battery thermal management design, operating-condition optimization, and lifetime safety assessment in locomotive systems. Focusing on the coupling between thermal behavior and aging behavior in lithium-ion batteries, this study aims to develop a coupled model integrating electrochemical behavior, thermal behavior, and SEI film growth. The main contributions of this work can be summarized as follows:

(1) An analytical framework for the thermal response and aging behavior of lithium-ion batteries is developed for the complex service characteristics of new-energy locomotive traction batteries, including high C-rates, wide temperature ranges, and long-term cycling. This framework addresses the limitation that conclusions derived from conventional automotive battery studies cannot be directly applied to locomotive traction batteries.

(2) An electrochemical-thermal-SEI film growth multi-physics coupled model is established by integrating a P2D electrochemical model, a three-dimensional heat conduction model, and an SEI film growth aging model, enabling the simultaneous analysis of key variables such as terminal voltage, temperature field, SEI film thickness, and capacity fade.

(3) The effects of different discharge rates and ambient temperatures on polarization heat generation, heat accumulation, SOH degradation, and SEI film growth are quantitatively revealed, and the coupled degradation mechanism among rate, temperature, and aging is clarified.

(4) The spatial nonuniformity of the coupled thermal-aging response within a single cell is analyzed from the perspective of spatial distribution. The enhancement of local temperature gradients under high-rate cycling and its potential influence on accelerated local aging are revealed, providing a theoretical basis for thermal management optimization and lifetime prediction of traction batteries for new-energy locomotives.

The remainder of this paper is organized as follows. Section 2 introduces the construction of the electrochemical-thermal-SEI film growth coupled model, with emphasis on the electrochemical reaction mechanism based on the P2D model, the thermal model based on energy conservation, and the SEI film growth aging model. Section 3 presents the model parameter settings and conducts simulation analyses of the thermal response and aging behavior of lithium-ion batteries from three aspects: different discharge rates, different ambient temperatures, and the internal spatial distribution within a single cell. Section 4 summarizes the main conclusions of this study, discusses the effects of rate, temperature, and spatial factors on the coupled thermal-aging behavior of the battery, and highlights their implications for thermal management design and lifetime assessment of traction batteries for new-energy locomotives.

2 Model construction

To construct an electrochemical-thermal-aging coupled model, the electrochemical, thermal, and aging processes must be integrated. The electrochemical part is based on the P2D model, which describes

lithium-ion transport in the solid and electrolyte phases, charge conservation, and interfacial reaction behavior. The thermal part adopts a three-dimensional heat conduction model to describe heat generation, diffusion, and heat exchange with the surrounding environment [17]. The aging part introduces a negative-electrode SEI growth submodel to characterize active lithium loss and interfacial impedance growth. Fig. 1 presents the overall framework of the proposed model.

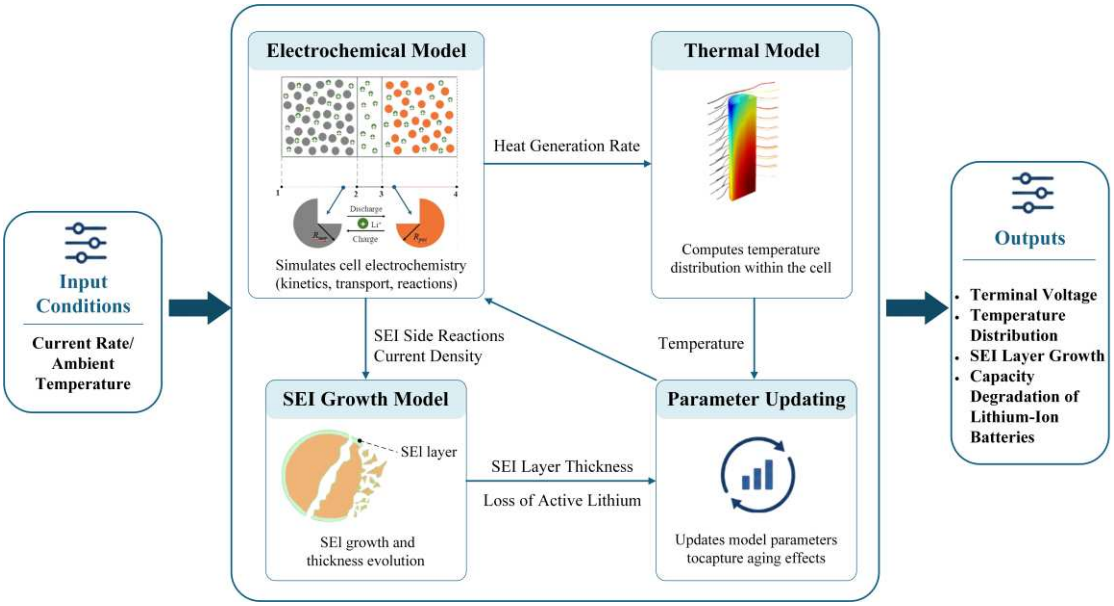


Fig. 1 Overall framework of the electrochemical-thermal-aging coupled model

With ambient temperature and charge-discharge rate as inputs, the model establishes a coupled system consisting of electrochemical, thermal, and SEI-aging modules. The electrochemical model serves as the core foundation by simulating internal electrochemical reactions and ion transport, and it provides the heat generation rate and SEI side-reaction current density. These outputs drive the thermal model for temperature-field calculation and the SEI aging model for film growth and active lithium loss. The thermal model feeds back temperature information, while the SEI aging model feeds back film thickness and lithium-loss information. Through the parameter-updating module, these feedbacks dynamically update the electrochemical model parameters, thereby realizing synchronous electrochemical-thermal-aging coupling and enabling the output of key indicators such as terminal voltage, temperature distribution, SEI film thickness, and capacity fade [18].

2.1 Electrochemical reaction mechanism based on the P2D model

The P2D model proposed by Doyle, Fuller, and Newman is adopted as the core electrochemical model. This model can simultaneously describe lithium-ion diffusion in solid particles, transport in the

electrolyte, electronic conduction, and electrochemical reactions at the electrode/electrolyte interface [19],[20], and it is one of the most widely used mechanistic models for lithium-ion batteries.

Fig. 2 illustrates the P2D model of a lithium-ion battery. Along the cell thickness direction, the battery can be divided into five regions: negative current collector, negative porous electrode, separator, positive porous electrode, and positive current collector [21],[22]. Both the negative and positive porous electrodes contain a large number of spherical active particles. Therefore, the model must solve concentration and potential distributions in the macroscopic thickness direction and solid-phase lithium-ion diffusion in the particle radial direction [23],[24], which gives rise to the term pseudo-two-dimensional.

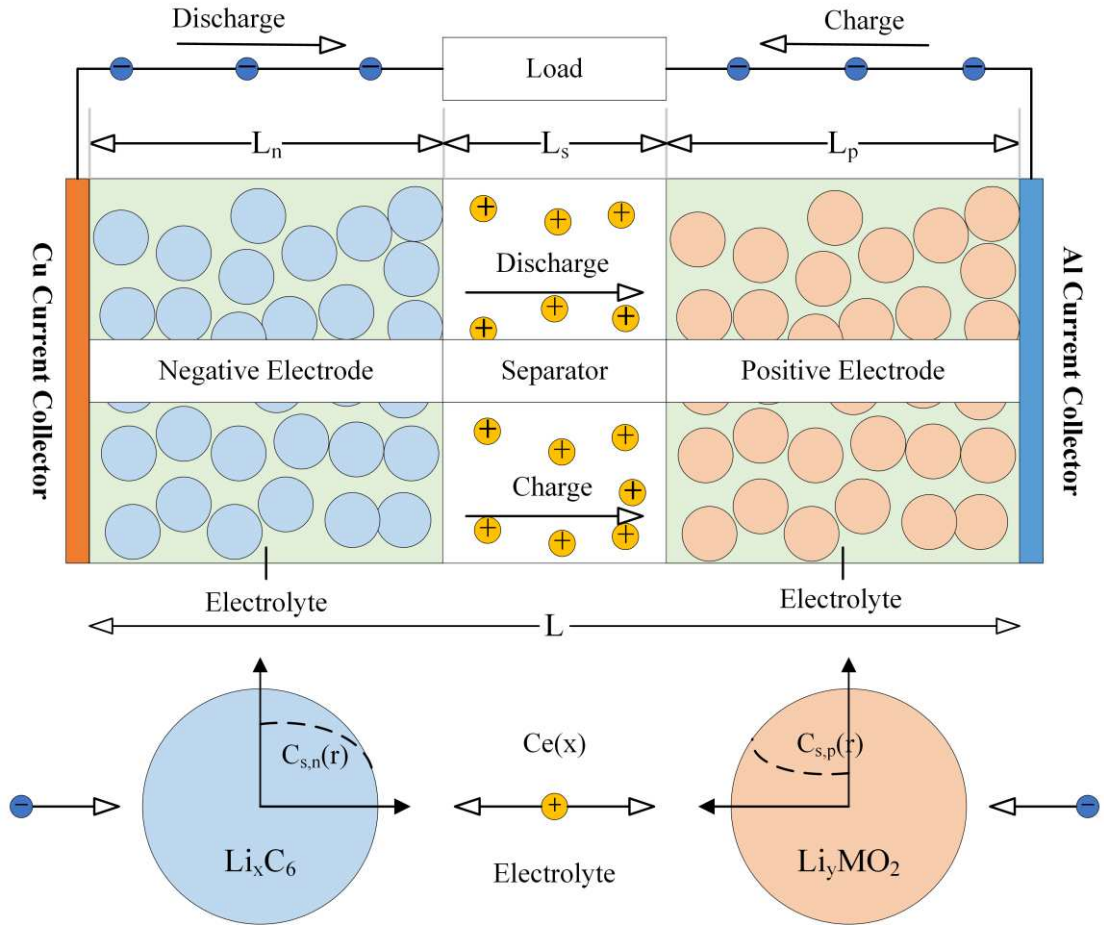


Fig. 2 Schematic diagram of the lithium-ion battery P2D model

Where *Ln*, *Ls*, and *Lp* denote the thicknesses of the negative electrode, separator, and positive electrode, respectively; *Ce(x)* denotes the electrolyte-phase lithium-ion concentration distributed along the cell thickness direction; *Cs,n(r)* and *Cs,p(r)* denote the radial solid-phase lithium concentrations in the negative and positive active particles, respectively; and LixC6 and LiyMO2 represent lithiated

graphite in the negative electrode and lithiated metal oxide in the positive electrode.

The mass conservation of lithium ions in the electrolyte is described by the modified Fick's second law, considering both diffusion and migration. The electrochemical reaction rate at the electrode/electrolyte interface is described by the Butler-Volmer equation [25][26][27]. The internal lithium-ion concentration, potential distribution, and interfacial current density can thereby be obtained, providing the basis for heat-generation calculation and aging modeling.

2.2 Three-dimensional Thermal Model

The internal thermal process of the battery is governed by the energy conservation equation [28]. A three-dimensional thermal model is adopted to more realistically capture local hotspots and temperature gradients. Based on Fourier's law and energy conservation [29], the transient temperature field *T(x, y, z, t)* inside the battery is described by Eq.(1):

$$\rho C_p \frac{\partial T}{\partial t} = \nabla \cdot (\lambda \nabla T) + \dot{q}_{gen} \tag{1}$$

where ρ is the average density of the battery material, *Cp* is the constant-pressure specific heat capacity, and λ is the thermal conductivity tensor. For anisotropic cell structures, the thermal conductivity may differ between the in-plane directions *(y, z)* and the thickness direction *(x)*. The volumetric heat generation rate $\dot{q}_{gen}$ is the key coupling term in the model.

The volumetric heat generation rate $\dot{q}_{gen}$ consists of reversible and irreversible heat effects produced during electrochemical processes. A locally resolved heat-generation model is used to directly relate the heat source to the local variables calculated by the P2D model [30],[31]. The total heat generation includes three components:

(1) Reaction heat (reversible heat) $\dot{q}_{rxn}$:

$$\dot{q}_{rxn} = ajT \frac{\partial U_{ref}}{\partial T} \tag{2}$$

This term represents the thermal effect associated with the entropy change of the electrochemical reaction.

(2) Polarization heat (activation heat) $\dot{q}_{polar}$:

$$\dot{q}_{polar} = aj\eta \tag{3}$$

This term is jointly determined by the local reaction current and overpotential and constitutes an important part of irreversible heat generation.

(3) Joule heat (ohmic heat) $\dot{q}_{joule}$:

$$\dot{q}_{joule} = \sigma^{eff}\left(\frac{\partial \phi_s}{\partial x}\right)^2 + \kappa^{eff}\left(\frac{\partial \phi_e}{\partial x}\right)^2 + \frac{2\kappa^{eff}RT}{F}(1-t_+^0)(1+\frac{\partial\, ln\, f_{\pm}}{\partial\, ln\, c_e})\frac{\partial\, ln\, c_e}{\partial x}\frac{\partial \phi_e}{\partial x} \quad (4)$$

where the parameter $f_{\pm}$ denotes the mean molar activity coefficient of the electrolyte. This term includes ohmic losses in both the electrolyte and the solid phase.

Accordingly, the total local heat generation rate is expressed as:

$$\dot{q}_{gen} = \dot{q}_{rxn} + \dot{q}_{polar} + \dot{q}_{joule} \quad (5)$$

The heat generation rate is determined from the local variables calculated by the P2D model and is used as the heat-source input for the three-dimensional thermal model.

The boundary condition of the thermal model is mainly described by Newton's law of cooling for convective heat dissipation [32],[33]:

$$-\lambda\frac{\partial T}{\partial n} = h(T_{surface} - T_{\infty}) \quad (6)$$

where n is the outward unit normal vector of the surface, h is the convective heat transfer coefficient determined by the cooling mode, and T_{∞} is the ambient temperature. Because radiative heat transfer has a relatively small influence under conventional operating conditions, only convective heat transfer is considered in the present model.

2.3 SEI growth aging model

To describe one of the dominant mechanisms of capacity fade in lithium-ion batteries, namely loss of lithium inventory (LLI) [34],[35], an SEI growth kinetic model is integrated on the negative-electrode side. The model is based on the following physical picture.

When the negative-electrode potential decreases to a sufficiently low level, solvent molecules in the electrolyte undergo reduction reactions on the negative-electrode surface, generating insoluble products that deposit on the electrode surface and form the SEI layer. Although the initially formed SEI layer can partly suppress further electrolyte decomposition, local mechanical stresses induced by lithiation and de-lithiation of negative-electrode particles during subsequent cycles may cause repeated SEI cracking, repair, and regeneration [36]**Error! Reference source not found.**[37][38], thereby continuously consuming active lithium and electrolyte.

The SEI growth model is an electrochemical-kinetics-based side-reaction model whose core is the definition of a side reaction occurring in parallel with the main intercalation reaction [39],[40]. The overpotential of this side reaction is defined as η_{SEI}:

$$\eta_{SEI} = \phi_s - \phi_e - U_{SEI} \tag{7}$$

where U_{SEI} is the thermodynamic equilibrium potential of the SEI formation reaction.

The local current density of the SEI side reaction, j_{SEI}, is described by a Tafel-type equation [41], assuming that the reaction is controlled by charge transfer and that the reverse reaction is negligible at high overpotential:

$$j_{SEI} = -a i_{0,SEI}\, exp\left(-\frac{\alpha_{c,SEI} F \eta_{SEI}}{RT}\right) \tag{8}$$

where $i_{0,SEI}$is the exchange current density of the SEI reaction. Similar to the main reaction, it can be assumed to be dependent on the electrolyte concentration:

$$i_{0,SEI} = F k_{SEI} c_e^{\alpha_{SEI}} \tag{9}$$

where $k_{\mathrm{SEI}}$is the rate constant of the SEI reaction, and $\alpha_{c,SEI}$is the cathodic transfer coefficient of the SEI reaction. The negative sign indicates that this side reaction is a reduction reaction.

2.3.1 Evolution of SEI film thickness

The growth rate of the SEI film is proportional to the side-reaction current density [42]. Assuming that the generated SEI product uniformly covers the surface of spherical particles, the evolution equation for SEI film thickness δ_{SEI} is given by Eq. (10):

$$\frac{d\delta_{SEI}}{dt} = -\frac{M_{SEI} j_{SEI}}{\rho_{SEI} F a} \tag{10}$$

where M_{SEI} is the average molar mass of the SEI film product, and ρ_{SEI} is the density of the SEI film. It can be inferred from this equation that a higher SEI side-reaction current leads to faster film growth [43],[44]. As cycling proceeds, δ_{SEI} continuously accumulates, thereby serving as an important state variable for characterizing the aging degree of the battery.

2.3.2 Aging feedback mechanism

Continuous SEI growth is not only an outcome of aging but also feeds back into the electrochemical and thermal behavior of the battery **Error! Reference source not found.**[45],[46], mainly in the following two aspects.

(1) Active lithium consumption: the SEI side reaction continuously consumes lithium ions and reduces the inventory of active lithium [47]. This process is represented by modifying the flux boundary condition at the negative-particle surface. In the original formulation, the surface lithium-ion flux is used

only for the main reaction. After introducing the SEI side reaction, the surface lithium flux must supply both the main reaction and the side reaction, giving:

$$-D_s \frac{\partial c_s}{\partial r}|_{r=R_s} = \frac{j + j_{SEI}}{F} \tag{11}$$

The side-reaction term reduces the amount of lithium ions available for the main intercalation/deintercalation reaction, which macroscopically manifests as a decrease in reversible capacity, namely battery capacity fade.

(2) Interfacial impedance increase: as the SEI film thickens, the resistance encountered by lithium ions when passing from the electrolyte through the film layer to the electrode surface gradually increases. If the ionic conductivity of the SEI film k_{SEI} is assumed to be constant, the interfacial impedance is approximately proportional to the film thickness [48]. To reduce model complexity, this effect is equivalently described in this study by modifying the exchange current density i_0 of the main negative-electrode reaction:

$$i_{0,mod} = \frac{i_0}{1 + (\delta_{SEI}/\delta_0)} \tag{12}$$

Under the same external current, a larger overpotential is required, leading to stronger polarization and increased heat generation.

3 Simulation and analysis

3.1 Parameter settings

An 8 Ah prismatic lithium-iron phosphate battery is selected as the research object, and the single-cell model is established as shown in Fig. 3.

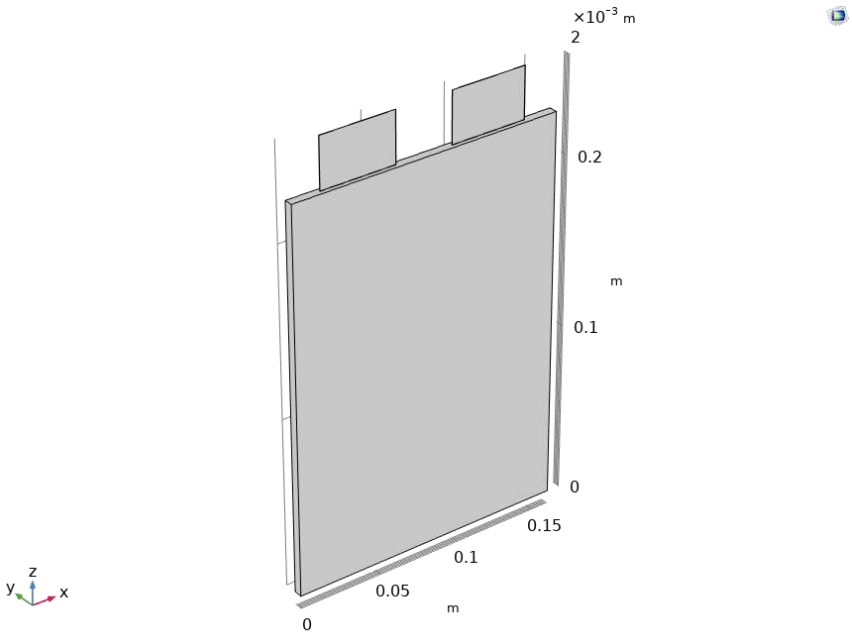


Fig. 3 Single-cell geometry model

The main geometric dimensions, including length, width, and height, are listed in Tab. 1.

Tab. 1 Battery model dimensions

Parameter	Length	Width	Height
Value (mm)	160	5	227

The main parameters of the P2D electrochemical model and the key parameters of the SEI growth aging model are listed in Tab. 2 and 3, respectively.

Tab. 2 Simulation parameters of the lithium-ion battery

Parameter	Unit	Negative electrode	Separator	Positive electrode
Electrode thickness	um	59	20	92
Active particle radius	um	10	--	1.15
Porosity	--	0.3	0.4	0.28
Volume fraction of active material	--	0.675	--	0.544
Maximum solid-phase lithium concentration	mol/m3	28688	--	20950
Solid-phase electronic conductivity	S/m	100	--	91
Bruggeman coefficient	--	1.5	2	1.5
Anodic/cathodic transfer coefficient	--	0.5	--	0.5
Lithium-ion transference number	--	0.363	0.363	0.363
Density	kg/m^3	2660	492	1500
Constant-pressure specific heat capacity	J/(kg K)	1437	1978	1260
Faraday constant	C/mol	96485	96485	96485
Reference temperature	K	298.15	298.15	298.15

Tab. 3 Key parameters of the SEI growth aging model

Parameter	Symbol	Unit	Value
SEI reaction equilibrium potential	U_{SEI}	V vs. Li/Li$^+$	0.4
SEI reaction rate constant	$k_{SEI,ref}$	m s^{-1}	1.0e^{-12}
SEI reaction activation energy	$E_{a,SEI}$	J mol^{-1}	50000
SEI reaction transfer coefficient	$\alpha_{c,SEI}$	--	0.5
SEI film density	ρ_{SEI}	kg m^{-3}	1700
Average molar mass of SEI film	M_{SEI}	kg mol^{-1}	0.1
Reference thickness parameter	δ_0	m	1e-9

3.2 Thermal-aging evolution under different discharge rates

The discharge rate is an important operating parameter affecting the thermal behavior and aging process of lithium-ion batteries. In this simulation, the ambient temperature is set to 25 °C, the same charging protocol is applied to the battery, and cycling simulations are conducted under different discharge-rate conditions (1C, 2C, and 4C). The results and analysis are presented below.

(1) Comparison of discharge voltage curves at the 1st and 1000th cycles under different discharge rates as shown in Fig. 4.

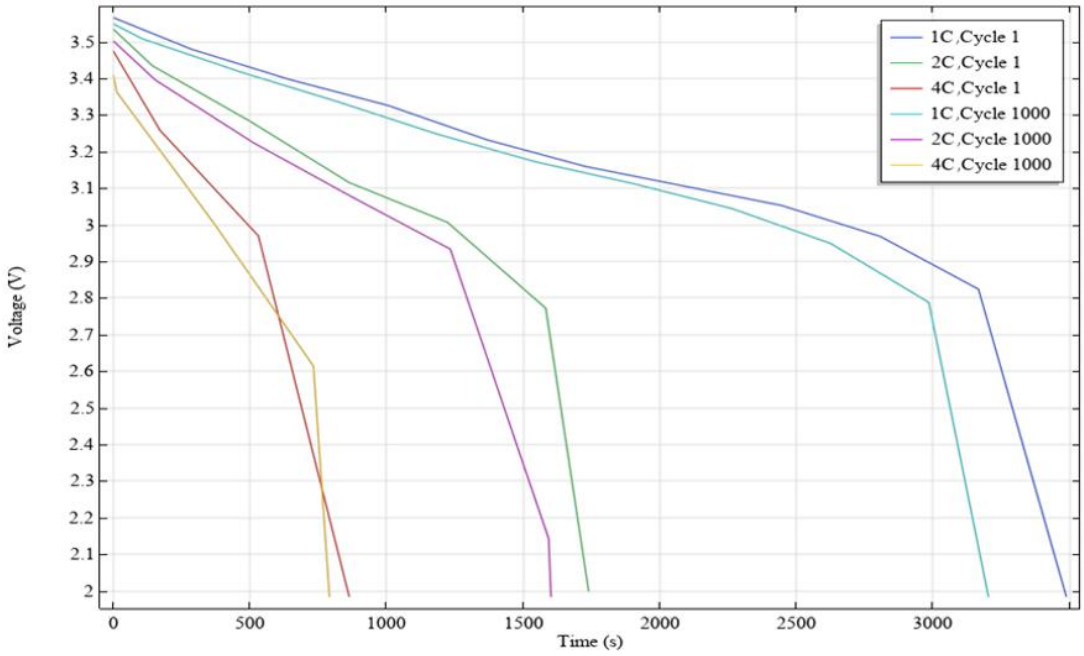


Fig. 4 Comparison of discharge voltage curves at the 1st and 1000th cycles under different discharge rates

In Fig. 4, the terminal voltage decreases gradually during discharge under all rate conditions. A higher discharge rate leads to a faster voltage drop and a shorter discharge duration. The voltage plateau is relatively long and the curve declines gently under 1C, whereas the voltage drop becomes more pronounced under 2C. Under 4C, the voltage plateau is substantially shortened, indicating that high-rate discharge intensifies internal polarization and causes the terminal voltage to reach the cut-off voltage

more rapidly.

Comparing the curves before and after cycling, all discharge curves shift leftward to varying degrees after 1000 cycles, indicating a decrease in releasable capacity. Under 1C, the effective discharge time decreases from 3166 s to 2984 s, corresponding to a capacity retention of 94.3%. Under 2C, it decreases from 1582 s to 1232 s, corresponding to a capacity retention of 77.9%, indicating more pronounced degradation. Under 4C, the discharge duration is shorter, and the aged voltage plateau declines further, demonstrating that high-rate discharge aggravates polarization and internal-resistance losses and reduces output stability.

(2) SOH evolution with cycle number under different discharge-rate conditions as shown in Fig. 5.

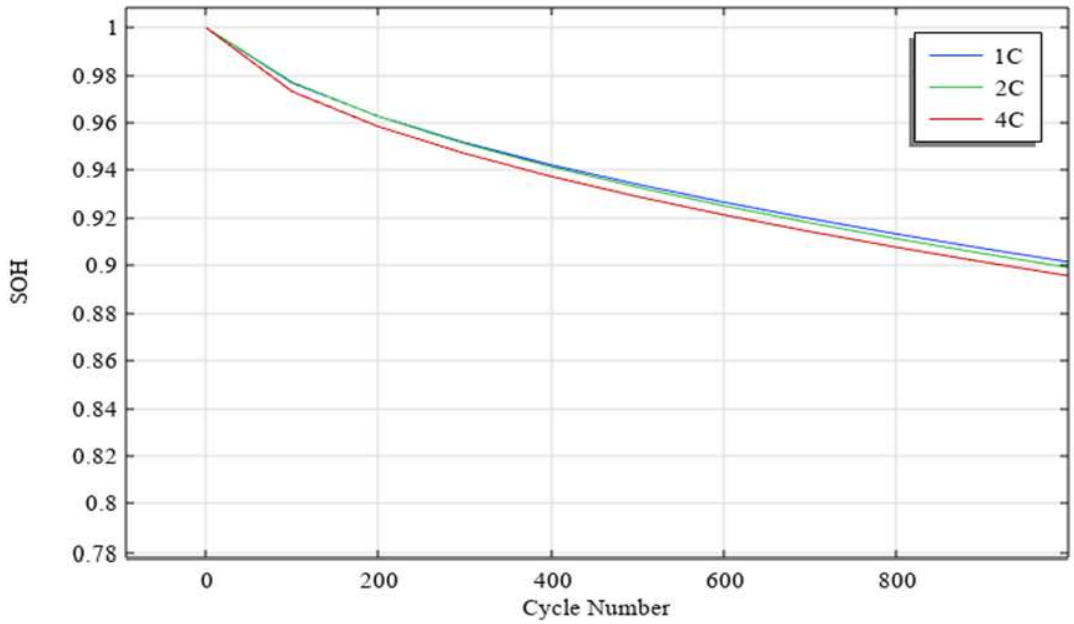


Fig. 5 SOH degradation curves under different discharge rates

In Fig. 5, the SOH decreases gradually with cycle number under all discharge rates. After 1000 cycles, the SOH values under 1C, 2C, and 4C are 0.902, 0.899, and 0.896, respectively, corresponding to capacity losses of 9.8%, 10.1%, and 10.4%. The largest SOH degradation occurs under 4C, whereas the smallest occurs under 1C, indicating that increasing the discharge rate accelerates battery health degradation to some extent. Over 1000 cycles, the average SOH loss per 100 cycles is 0.98%, 1.01%, and 1.04% for 1C, 2C, and 4C, respectively, and the overall degradation under 4C is approximately 1.06 times that under 1C. The three curves show a monotonic downward trend, confirming continuous health degradation during cycling. Although the difference among the curves is relatively small within the present operating range, the SOH values follow the order 4C < 2C < 1C at the same cycle number. High-

rate charge-discharge enhances internal polarization, increases reaction heat and ohmic heat generation, and accelerates SEI growth on the negative-electrode surface, thereby increasing active lithium consumption. Overall, the figure shows that high-rate operation aggravates capacity fade, although the SOH difference among the investigated rates remains limited.

(3) Average battery temperature under different discharge rates as shown in Fig. 6.

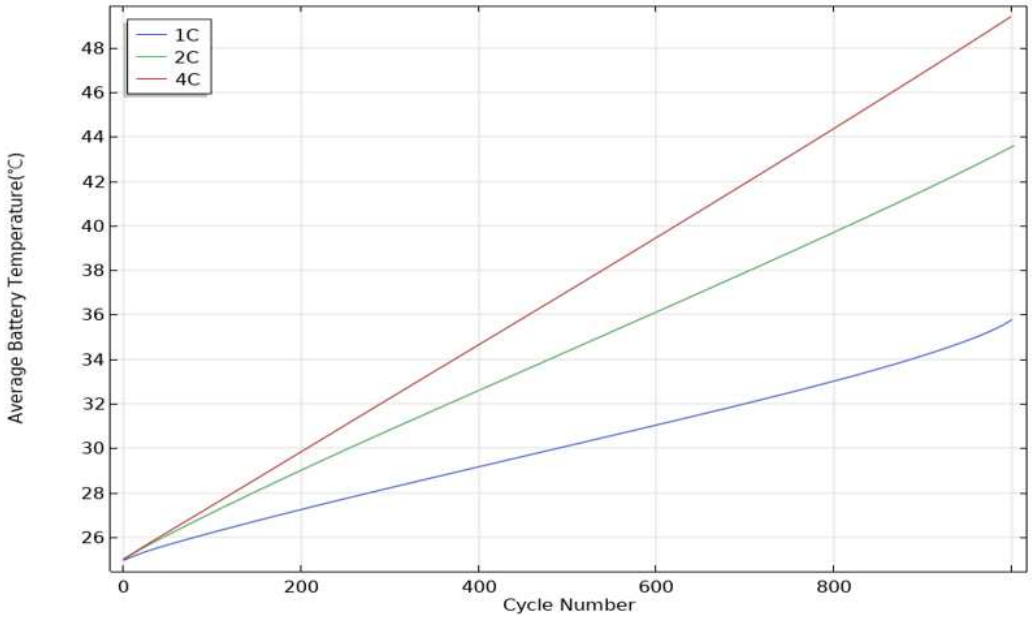


Fig. 6 Average battery temperature variation under different discharge rates

In Fig. 6, the average battery temperature increases with cycle number under all discharge rates, and the temperature rise becomes more evident at higher rates. The 4C curve remains the highest, indicating the most severe heat generation under high-rate operation, while the 1C curve increases most slowly and exhibits better thermal control. The initial average temperature is 25 °C for all three cases. After 1000 cycles, the average temperatures under 1C, 2C, and 4C increase to 35.8 °C, 43.5 °C, and 49.4 °C, corresponding to temperature rises of 10.8 °C, 18.5 °C, and 24.4 °C, respectively. The average temperature-rise rates per 100 cycles are 1.08 °C, 1.85 °C, and 2.44 °C for 1C, 2C, and 4C, respectively. The temperature-rise rate under 2C is approximately 1.71 times that under 1C, while that under 4C is approximately 2.26 times that under 1C. These results show that high-rate operation significantly enhances internal heat generation and heat accumulation.

(4) SEI thickness evolution with cumulative time under different discharge rates as shown in Fig. 7.

SEI film thickness is an important internal variable for characterizing the aging state of lithium-ion batteries, and its growth reflects the accumulation of side reactions at the negative-electrode interface.

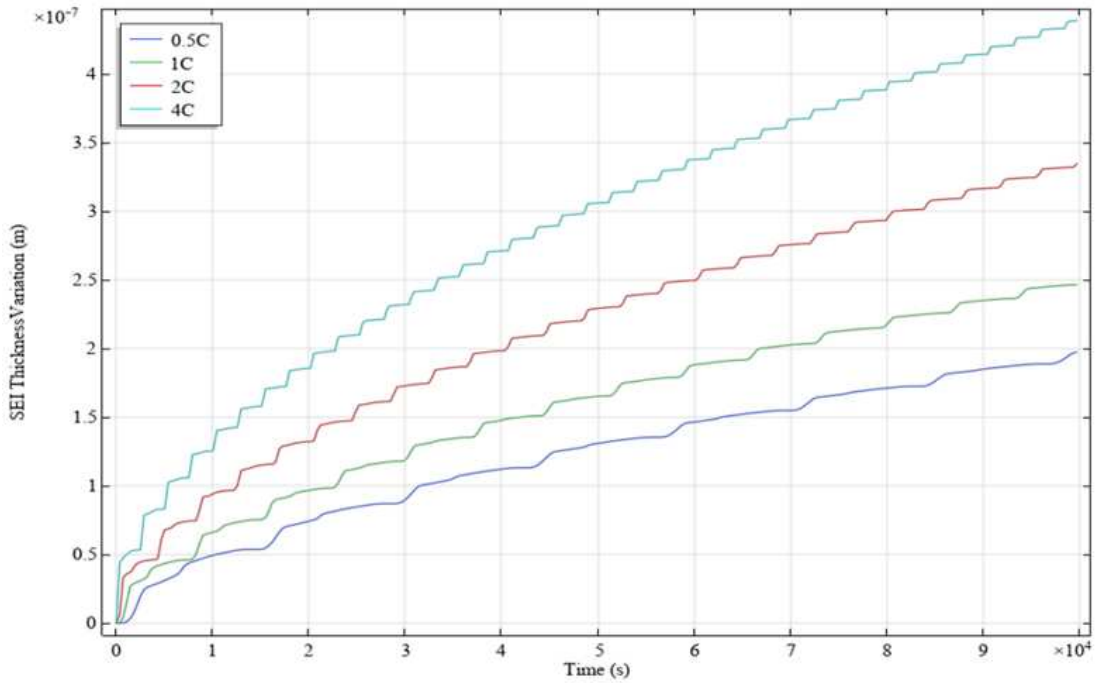


Fig. 7 SEI thickness variation with cumulative time under different discharge rates

In Fig. 7, the SEI thickness increases continuously with time under all discharge rates, and the growth becomes more pronounced as the rate increases. The curves are not perfectly smooth but exhibit a step-like growth pattern, suggesting that SEI thickening is associated with charge-discharge cycling: the SEI film grows during each cycle or during specific electrochemical stages and then enters a relatively slower growth stage. In terms of the growth trend, the SEI film grows rapidly at the early stage and then the growth rate gradually decreases. Initially, strong side reactions occur between the negative-electrode surface and the electrolyte, leading to rapid SEI formation. As the SEI film thickens, the diffusion resistance for lithium ions and solvent molecules increases, suppressing the side reaction to some extent and slowing down the growth rate.

At 10×10^4 s, the SEI thickness increments under 0.5C, 1C, 2C, and 4C are 1.97×10^{-7} m (197 nm), 2.47×10^{-7} m (247 nm), 3.35×10^{-7} m (335 nm), and 4.39×10^{-7} m (439 nm), respectively. The SEI increment under 4C is approximately 2.23 times that under 0.5C, indicating that high-rate operation significantly accelerates SEI growth. Taking 10×10^4 s as the calculation time, the average SEI growth rates under 0.5C, 1C, 2C, and 4C are estimated as 1.97×10^{-3} nm/s, 2.47×10^{-3} nm/s, 3.35×10^{-3} nm/s, and 4.39×10^{-3} nm/s, respectively. These results indicate that high-rate charge-discharge enhances polarization and heat generation, promotes side reactions at the negative-electrode interface, and accelerates battery aging.

3.3 Thermal-aging evolution under different ambient temperatures

Temperature variation affects not only the transient thermal response of the battery but also the long-term degradation trajectory by regulating reaction kinetics, ion-transport properties, and side-reaction rates.

(1) SOH evolution under different ambient temperatures as shown in Fig. 8.

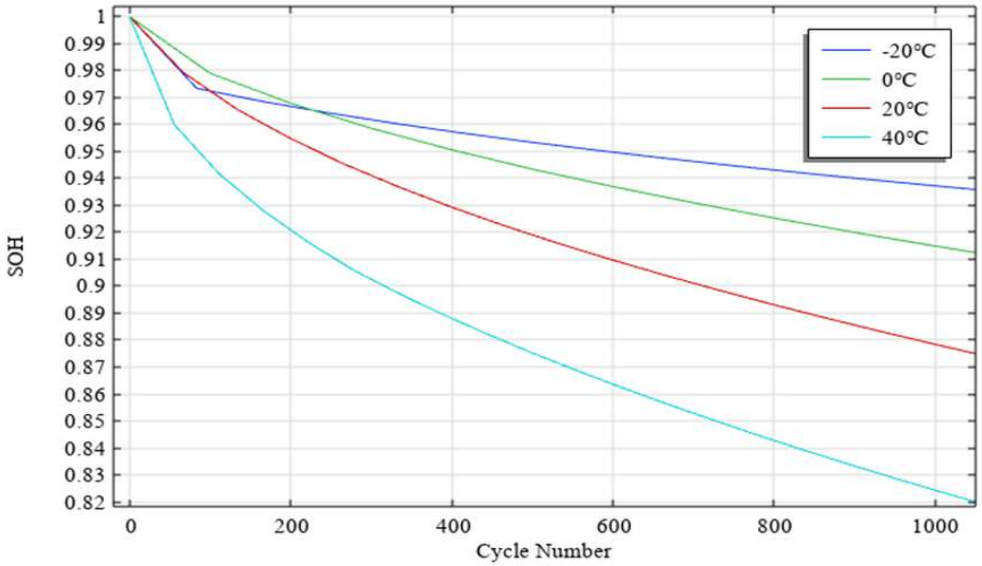


Fig. 8 SOH degradation curves under different ambient temperatures

As the ambient temperature increases, SOH degradation becomes significantly faster. After 1000 cycles, the SOH under 40 °C is only 0.824, which is approximately 11.3 percentage points lower than that under -20 °C, demonstrating that high temperature substantially accelerates battery health degradation. Taking the -20 °C case as the reference, the SOH loss under 40 °C within 1000 cycles is approximately 2.8 times larger. Compared with the 20 °C case, the SOH loss under 40 °C is approximately 1.44 times larger. High temperature not only increases internal reaction rates but also promotes continuous SEI growth, strengthens side reactions, and increases active lithium loss, thereby accelerating the decrease in capacity retention. From the curves, the SOH at 200 cycles under 40 °C has already decreased to 0.921, whereas those under -20 °C and 0 °C remain around 0.967, indicating that early-stage degradation is more pronounced at high temperature. Taking SOH = 0.9 as a representative degradation threshold, the 40 °C case reaches this threshold at 316 cycles, while the 20 °C case reaches it at approximately 712 cycles. The low-temperature cases do not decrease below 0.9 within 1000 cycles. Overall, all four curves decrease gradually with increasing cycle number, indicating continuous capacity fade. The degradation severity follows the order 40 °C > 20 °C > 0 °C > -20 °C; in other words, a higher

temperature results in faster SOH degradation.

(2) SEI thickness evolution during a single cycle under different initial temperatures as shown in Fig. 9.

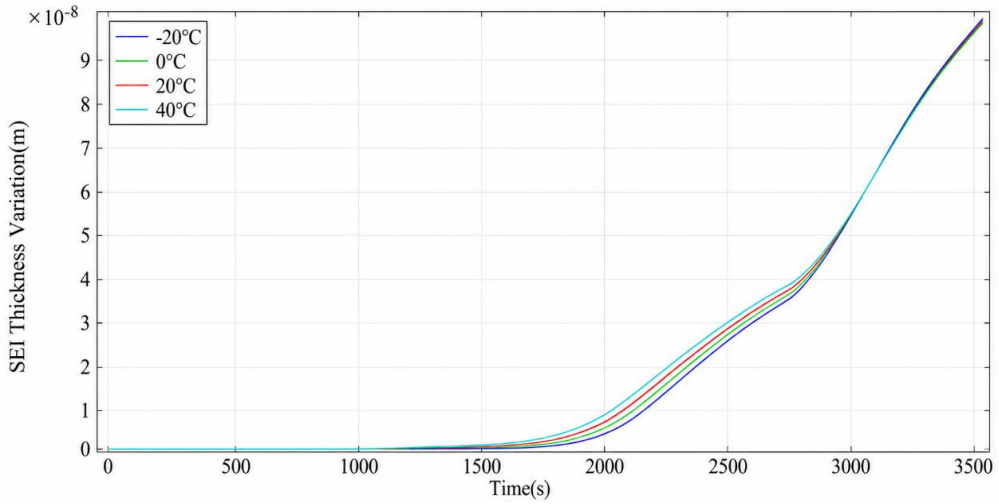


Fig. 9 SEI thickness growth curves under different ambient temperatures

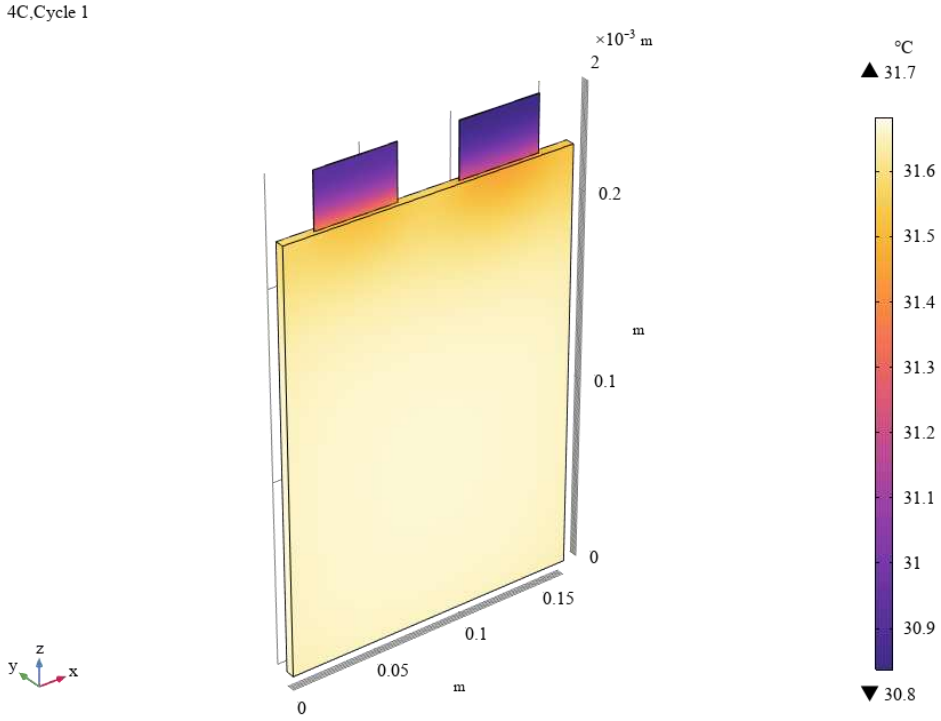
As shown in Fig. 9, the SEI thickness variation increases with discharge time under all ambient temperatures and exhibits a clear staged growth pattern. During 0-1500 s, the SEI thickness changes only slightly. During 1500-2800 s, the SEI begins to grow appreciably, and the growth rate increases with temperature. After 2800 s, the SEI thickness increases rapidly, and the final thickness variation under all four temperatures approaches 1.0 × 10^-7 m. In the figure, a value of 1 on the vertical axis corresponds to 1 × 10^-8 m, namely 10 nm. During the early-to-middle discharge stage, the temperature effect on SEI growth is relatively evident, following the order 40 °C > 20 °C > 0 °C > -20 °C. At the end of discharge, the thickness variation under -20 °C, 0 °C, 20 °C, and 40 °C is approximately 9.8-9.9 × 10^-8 m, corresponding to 98-99 nm. These results indicate that high temperature accelerates SEI growth during the middle stage of discharge, although the final SEI thickness variation after this single discharge process differs only slightly among the investigated temperatures.

3.4 Thermal-aging inconsistency within a single cell: spatial effects of thermal-aging coupling

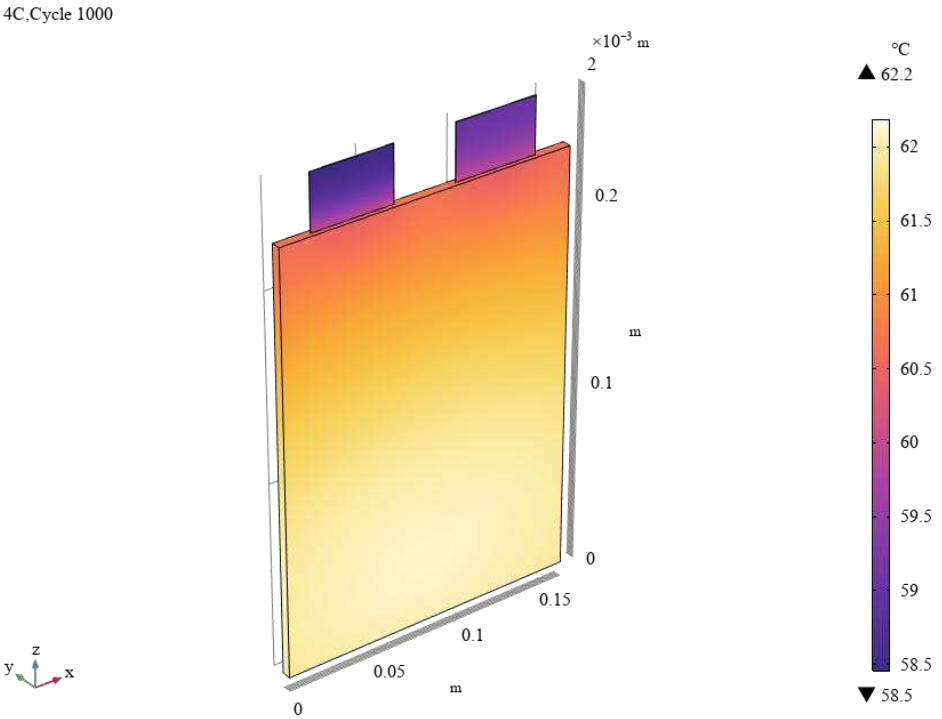
Both high discharge rate and high ambient temperature enhance heat generation and accelerate SEI side reactions, thereby strengthening the coupled thermal-aging effect. However, this coupling not only affects the overall capacity fade and temperature rise of the cell but may also induce spatial differentiation in thermal state and aging tendency among different internal regions.

Fig. 10 compares the internal temperature distributions at the end of discharge for the 1st and 1000th

cycles under the 4C condition.



(a) 4C, 1st cycle



(b) 4C, 1000th cycle

Fig. 10 Internal temperature distributions of the battery under 4C at the 1st and 1000th cycles

The temperature distribution contours under 4C at the 1st and 1000th cycles show that both the overall temperature level and temperature nonuniformity increase markedly with cycling. The cell body

exhibits a higher temperature, whereas the regions near the tabs and the upper edge remain relatively cooler, indicating that heat generation and diffusion are jointly affected by local heat-generation intensity, structural position, and heat-dissipation conditions. At the 1st cycle, the battery temperature ranges from 30.8 °C to 31.7 °C, with a maximum temperature difference of 0.9 °C, and the temperature distribution in the body region is relatively uniform. At the 1000th cycle, the temperature range increases to 58.5~62.2 °C, and the maximum temperature difference increases to 3.7 °C. The average temperature of the cell body rises from 31.2 °C to 60.3 °C, corresponding to an average temperature rise of 29.1 °C. The temperature nonuniformity coefficient I_T is defined as:

$$I_T = \frac{T_{max} - T_{min}}{T_{avg}} \tag{13}$$

where T_{max}, T_{min}, and T_{avg} denote the maximum temperature, minimum temperature, and average temperature of the cell body, respectively.

Further calculation shows that the temperature nonuniformity coefficient increases from 2.9% at the 1st cycle to 6.1% at the 1000th cycle, approximately 2.1 times the initial value. This result indicates that 4C high-rate cycling not only causes pronounced heat accumulation but also enhances the spatial nonuniformity of the internal temperature distribution, which may further accelerate SEI growth, active lithium loss, and local aging.

4 Conclusions

Based on the constructed electrochemical-thermal-SEI growth coupled single-cell model, simulations are conducted under different discharge rates and ambient temperatures. The potential spatial nonuniformity of coupled thermal-aging behavior within the cell is further analyzed. The main conclusions are as follows:

(1) As the discharge rate increases from 1C to 4C, the terminal voltage drops more rapidly, the discharge duration is shortened, and the discharge curves shift leftward after cycling, indicating a decrease in releasable capacity. The capacity losses under 1C, 2C, and 4C are 9.8%, 10.1%, and 10.4%, respectively, showing faster degradation at higher rates. The average temperatures under 1C, 2C, and 4C all exceed 35 °C, and the temperature-rise rate under 4C is approximately 2.26 times that under 1C, indicating that high-rate operation significantly enhances heat accumulation. In terms of SEI growth, the SEI thickness increment under 4C is 2.23 times that under 0.5C. As cycling proceeds, the growth of interfacial impedance further feeds back into heat generation, forming a positive feedback loop between

heat accumulation and aging reactions. Overall, high-rate operation not only intensifies electrochemical polarization but also substantially enhances internal heat generation and heat accumulation, thereby accelerating SEI side reactions.

(2) The simulation results show that the SOH under 40 °C degrades faster in the early stage, leading to a significantly shortened cycle life and the most severe aging behavior. After cycling, the SOH under 40 °C is approximately 11.3 percentage points lower than that under -20 °C, and the SOH loss is about 2.8 times that under -20 °C and 1.44 times that under 20 °C. When SOH = 0.9 is used as the degradation threshold, the 40 °C condition reaches this threshold earliest. The SEI thickness increases with discharge time under all temperatures, and the influence of temperature is most pronounced during the middle stage of discharge; in comparison, the fastest SEI growth occurs under 40 °C. These findings indicate that high temperature increases the rate of internal side reactions, accelerates SEI growth, increases active lithium loss, and significantly shortens cycle life.

(3) The temperature distribution results show that 4C high-rate cycling simultaneously increases the temperature level and temperature nonuniformity of the battery. During the first cycle, the maximum temperature difference is small, the temperature nonuniformity coefficient is 2.9%, and the distribution is relatively uniform. After cycling, the temperature difference increases, the average temperature of the cell body rises sharply to 60.3 °C, and the temperature nonuniformity coefficient becomes 2.1 times its initial value. The cell body exhibits a higher temperature, whereas the tab and upper-edge regions remain relatively cooler, indicating that the temperature distribution is jointly controlled by local heat generation, structural position, and heat-dissipation conditions. Overall, long-term 4C cycling not only produces pronounced heat accumulation but also amplifies internal temperature gradients and promotes the formation of local high-temperature regions, thereby accelerating SEI growth, active lithium loss, and local aging.

This study provides a theoretical basis for suppressing the positive feedback between heat accumulation and aging reactions, delaying capacity fade, and extending the cycle life of traction batteries for new-energy locomotives.

Acknowledgements This work is supported by a confidential Overseas Young Talents Project on key technologies for the durability of on-board power batteries.

References：

[1]. Sharma, Mukul, Alholaisi, Arafa A.Alshahrani, M. D., et al. Advances in lithium-ion batteries: graphene anodes and lithium iron phosphate cathodes[J]. Ionics, 2025, 31, (12):12523-12544.

[2]. L. Xu, X. Lin, Y. Xie, X. Hu, Enabling high-fidelity electrochemical P2D modeling of lithium-ion batteries via fast and non-destructive parameter identification, Energy Storage Mater. 45(2022) 952–968.

[3]. Z. Chen, D.L. Danilov, R.A. Eichel, P.H.L. Notten, Porous electrode modeling and its applications to Li-ion batteries, Adv. Energy Mater. 12(2022)2201506.

[4]. L. Wang, C. Pan, L. Liu, Y. Cheng, X. Zhao, On-board state of health estimation of LiFePO4 battery pack through differential voltage analysis, Appl. Energy 168(2016)465–472.

[5]. Lu, Zehui, Tu, Hao, Fang, Huazhen, et al. Integrated optimal fast charging and active thermal management of lithium-ion batteries in extreme ambient temperatures[J]. IEEE Transactions on Control Systems Technology, 2025, 33(2):714-728.

[6]. Antonio G, Javier S M, Rafael S L, et al. Numerical analysis of kinetic mechanisms for battery thermal runaway prediction in lithium-ion batteries[J]. International Journal of Engine Research, 2022, 23(10):1691-1707.

[7]. Wei Shen, Ning Wang, Jun Zhang, et al. Heat generation and degradation mechanism of lithium-ion batteries during high-temperature aging[J]. ACS Omega, 2022, 7, (49):44733-44742.

[8]. Feng, Xuning, He, Xiangming, Ouyang, Minggao, et al. A coupled electrochemical-thermal failure model for predicting the thermal runaway behavior of lithium-ion batteries[J]. Journal of The Electrochemical Society, 2018, 165, (16): A3748-A3765.

[9]. Zeng, Liang, Jiang, Ziyue, Wang, Shanshan. Remaining useful life prediction of lithium-ion batteries based on MWASFormer network[J]. Ionics, 2026, 32, (1):503-522.

[10]. Yao, Yongming, Li, Fei, Li, Haofa, et al. State-of-health estimation of lithium-ion batteries based on QPSO-BPNN[J]. Ionics, 2025, 31, (2):1437-1449.

[11]. Shiqin Chen, Qi Zhang, Facheng Wang, et al. An electrochemical-thermal-aging effects coupled model for lithium-ion batteries performance simulation and state of health estimation[J]. Applied Thermal Engineering, 2024, 239.

[12]. Wang, Jie, Chen, Yihao, Mei, Yufei, et al. Influence of aging on thermal runaway behavior of lithium-ion batteries: experiments and simulations for engineering education[J]. Fire, 2025, 8, (12).

[13]. Jaguemont, Joris, Boulon, Loic, Venet, Pascal, et al. Lithium-ion battery aging experiments at subzero temperatures and model development for capacity fade estimation[J]. IEEE Transactions on Vehicular Technology, 2016, 65, (6):4328-4343.

[14]. Zeyang Geng, Siyang Wang, Matthew J. Lacey, et al. Bridging physics-based and equivalent circuit models for lithium-ion batteries[J]. Electrochimica Acta, 2021, 372.

[15]. Y. Li, J. Li, Y. Wang, et al. Research on lithium plating boundary characteristics and fast charging strategy of lithium-ion batteries under high C-rate[J]. Journal of Energy Storage, 2026, 154.

[16]. Luo, Yufu, Li, Peichao, Zhang, Xiaoqiang, et al. Physics-based electrochemical-thermal-mechanical-side reaction coupling aging model for lithium-ion batteries[J]. Journal of Electronic Materials, 2025, 54, (6):4618-4634.

[17]. Tripathi, Piyush Mani, Marconnet, Amy M. Multi-physics numerical analysis of single-phase immersion cooling for thermal management of li-ion batteries[J]. arXiv, 2024.

[18]. Zhang, Xingbo, Chen, Kui, Luo, Yang, et al. Battery capacity degradation prediction based on singular spectrum analysis and improved deep learning[J]. Ionics, 2025, 31, (10):10527-10535.

[19]. Bai, Xuanyao, Peng, Donghong, Chen, Yanxia, et al. Three-dimensional electrochemical-magnetic-thermal coupling model for lithium-ion batteries and its application in battery health monitoring and fault diagnosis[J]. Scientific Reports, 2024, 14, (1):1-18.

[20]. Bowen Zheng, Zhichao Deng, Zhenhao Luo, et al. A comprehensive review of lithium-ion battery modelling research and prospects: in-depth analysis of current research and future directions[J]. Applied Energy, 2025, 401, Part B.

[21]. Kumar, Vinod, Sharma, Ashwini Kumar. Modified pseudo-two-dimensional model for spiral-wound cylindrical lithium-ion batteries[J]. Journal of The Electrochemical Society, 2025, 172, (5):050507-05050.

[22]. Yuxuan Gu, Jianxiao Wang, Yuanbo Chen, et al. A simplified electro-chemical lithium-ion battery model applicable for in situ monitoring and online control[J]. Energy, 2023, 264.

[23]. Hussain, Arif, Mao, Zhiyu, Li, Mei, et al. A comprehensive review of the pseudo-two-dimensional (P2D) model: model development, solutions methods, and applications[J]. Advanced Theory and Simulations, 2025, 8, (5)6.

[24]. Elia Zonta, Ivana Jovanovic Buha,Michele Spinola, et al. Time-dependent global sensitivity analysis of the Doyle–Fuller–Newman model[J]. Journal of Energy Storage, 2026, 158.

[25]. Myeong-Su Lee, Jaemin Oh, Dong-Chan Lee, et al. Forward and inverse simulation of pseudo-two-dimensional model of lithium-ion batteries using neural networks[J]. Computer Methods in Applied Mechanics and Engineering, 2025, 438, Part B.

[26]. Haghverdi, Keivan, Danilov, Dmitri L. Mulder, Grietus, et al. Joint dynamics and efficient initialization techniques for potentials and currents in the P2D battery model[J]. Scientific Reports, 2025, 15, (1):1-14.

[27]. Kim, Minsu, Schaeffer, Joachim, Berliner, Marc D., et al. Accounting for the effects of probabilistic uncertainty during fast charging of lithium-ion batteries[J]. arXiv, 2024.

[28]. Luigi Mattia, Hamzeh Beiranvand, Walter Zamboni, et al. Lithium-ion battery thermal modelling and characterisation: a comprehensive review[J]. Journal of Energy Storage, 2025, 12.

[29]. Chengzhi Wu, Mingyun Tang, Wei Peng, et al. Study on the impact of temperature-dependent anisotropic thermal conductivity on thermal diffusion in lithium-ion batteries[J]. Journal of Power Sources, 2024, 62.

[30]. Jiaxing Yang, Hengyun Zhang, Yidong Xu, et al. Analysis of heat generation in lithium-ion battery components and voltage rebound based on electrochemical and thermal coupled model[J]. Journal of Energy Storage, 2023, 72, Part C.

[31]. Dix, Sean T.Lowe, Jeffrey S.Avei, Mehdi Rashvand, et al. Leveraging molecular dynamics to improve porous electrode theory modeling predictions of lithium-ion battery cells[J]. Journal of The Electrochemical Society, 2023, 170, (8):083503-083503.

[32]. Domalanta, Marcel Roy B.Paraggua, Julie Anne D. R.A. Multiphysics model simulating the electrochemical, thermal, and thermal runaway behaviors of lithium polymer battery[J]. Energies, 2023, 16, (6).

[33]. Wang, Bo, Jiao, Changzhi, Zhang, Shiheng. Numerical improvement of battery thermal

management integrating phase change materials with fin-enhanced liquid cooling[J]. Energies, 2025, 18, (9).

[34]. Lv, Zhe, Si, Huinan, Yang, Zhe, et al. Simplified mechanistic aging model for lithium-ion batteries in large-scale applications[J]. Materials, 2025, 18, (6):134.

[35]. Sina Navidi, Adam Thelen, Tingkai Li, et al. Physics-informed machine learning for battery degradation diagnostics: A comparison of state-of-the-art methods[J]. Energy Storage Materials, 2024, 68.

[36]. Sart Ratanaporn, Kiettipong Banlusan. Dynamic evolution and degradation of silicon–electrolyte interfaces under cycling via chemical potential–controlled molecular dynamics[J]. ACS Applied Materials and Interfaces, 2026, 18, (9):13732-13742.

[37]. Yaqi Li, Wendi Guo, Daniel-Ioan Stroe, et al. Evolution of aging mechanisms and performance degradation of lithium-ion battery from moderate to severe capacity loss scenarios[J]. Chemical Engineering Journal, 2024, 498.

[38]. Narayan, Rekha, Laberty-Robert, Christel, Pelta, Juan, et al. Self-Healing: An emerging technology for next-generation smart batteries[J]. Advanced Energy Materials, 2022, 12, (17).

[39]. Junfu Li, Xueli Hu, Tongxin Li. Simulation of solid electrolyte interphase growth for lithium batteries based on kinetic monte carlo[J]. Energy Material Advances, 2024, 5, (1):1-15.

[40]. Yuanyuan Xie, Jianyang Li, Chris Yuan. Multiphysics modeling of lithium-ion battery capacity fading process with solid-electrolyte interphase growth by elementary reaction kinetics[J]. Journal of Power Sources, 2014, 248, 172-179.

[41]. Vykhodtsev, Anton V. Jang, Darren, Wang, Qianpu, et al. A review of lithium-ion battery models in techno-economic analyses of power systems[J]. arXiv, 2021.

[42]. Das, Supratim, Attia, Peter M.Chueh, William C., et al. Electrochemical kinetics of sei growth on carbon black: part ii. Modeling[J]. Journal of The Electrochemical Society, 2019, 166, (4): E107-E118.

[43]. Sodeyama, Keitaro. First-principles molecular dynamics study for SEI film formation mechanism of lithium-ion batteries[J]. Abstracts Of Papers of The American Chemical Society, 2019, 257.

[44]. Madi Reddy, Shiv Krishna, Shang, Wei, White, Ralph E. Mathematical model for sei growth

under open-circuit conditions[J]. Journal of The Electrochemical Society, 2022, 169, (9):090505-090505.

[45]. Carelli, Serena, Bessler, Wolfgang G. Coupling lithium plating with sei formation in a pseudo-3d model: a comprehensive approach to describe aging in lithium-ion cells[J]. Journal of The Electrochemical Society, 2022, 169, (5):050539-050539.

[46]. Wickramanayake, Toshan, Javadipour, Mehrnaz, Mehran, Kamyar. A novel solver for an electrochemical-thermal ageing model of a lithium-ion battery[J]. Batteries, 2024, 10, (4).

[47]. Luo, Guoqing, Zhang, Yongzhi, Tang, Aihua. Capacity degradation and aging mechanisms evolution of lithium-ion batteries under different operation conditions[J]. Energies, 2023, 16, (10).

[48]. Li, Wenlong, Sun, Tianxiao, Shah, Sameep Rajubhai, et al. Direct optical observation of solid electrolyte interphase formation dynamics in lithium-ion batteries[J]. Proceedings of the National Academy of Sciences, 2026, 123, (10).